JACS
JOURNAL OF THE AMERICAN CHEMICAL SOCIETY
pubs.acs.org/JACS
Article

Large-Area Conductive MOF Ultrathin Film Controllably Integrating Dinuclear-Metal Sites and Photosensitizers to Boost Photocatalytic CO_2 Reduction with H_2O as an Electron Donor

Kuo Yuan,*[,∇] Keying Tao,[∇] Tianqun Song,[∇] Ying Zhang, Tao Zhang, Fei Wang, Shuming Duan, Zheng Chen, Lujiang Li, Xiaotao Zhang, Dichang Zhong,* Zhiyong Tang, Tong-Bu Lu,* and Wenping Hu*

Cite This: *J. Am. Chem. Soc.* 2024, 146, 6893−6904

ABSTRACT: Owing to the electrical conductivity and periodic porosity, conductive metal−organic framework (cMOF) ultrathin films open new perspectives to photocatalysis. The space-selective assembly of catalytic sites and photosensitizers in/on cMOF is favorable for promoting the separation of photogenerated carriers and mass transfer. However, the controllable integration of functional units into the cMOF film is rarely reported. Herein, via the synergistic effect of steric hindrance and an electrostatic-driven strategy, the dinuclear-metal molecular catalysts (DMC) and perovskite (PVK) quantum dot photosensitizers were immobilized into channels and onto the surface of cMOF ultrathin films, respectively, affording [DMC@cMOF]-PVK film photocatalysts. In this unique heterostructure, cMOF not only facilitated the charge transfer from PVK to DMC but also guaranteed mass transfer. Using H_2O as an electron donor, [DMC@cMOF]-PVK realized a 133.36 μmol·g^{-1}·h^{-1} CO yield in photocatalytic CO_2 reduction, much higher than PVK and DMC-PVK. Owing to the excellent light transmission of films, multilayers of [DMC@cMOF]-PVK were integrated to increase the CO yield per unit area, and the 10-layer device realized a 1115.92 μmol·m^{-2} CO yield in 4 h, which was 8-fold higher than that of powder counterpart. This work not only lightens the development of cMOF-based composite films but also paves a novel avenue for an ultrathin film photocatalyst.

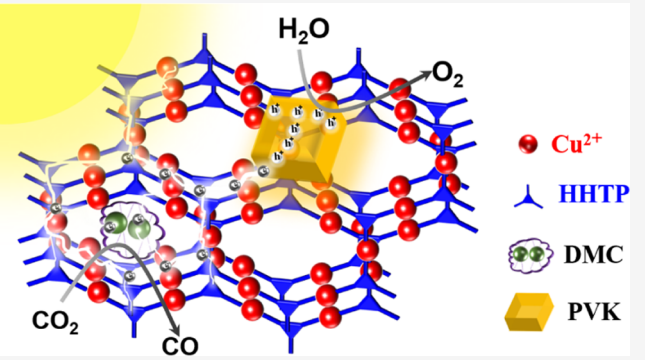

INTRODUCTION

As an emerging material, conductive metal−organic frameworks (cMOFs) possess multifarious charming characteristics, such as a periodic channel structure, an adjustable band gap, electrical conductivity, chemical diversity, and so on.[1] Among these characteristics, the excellent electrical conductivity of cMOF overcomes the long-time dilemma of electrically insulating properties in traditional MOFs and hence attracts widespread attention.[2] The application of MOFs is no longer limited to catalysis, separation, gas storage, luminescence, and other traditional fields.[3−7] Moreover, as an electrically active material, cMOF opens new perspectives for electrically related applications, such as field-effect transistors, photodetectors, electrical-resistance sensors, flexible electronics, electrocatalysis, batteries, and others.[8−14] In decades, cMOF-based devices have been developed a lot and accept wide attention in numerous fields.[15] Prior to the design of functional devices, it is urgent and crucial to synthesize a large-area cMOF film with high quality, *e.g.*, the crystalline degree, orientation, thickness, roughness, and others.[16−21] Among the various synthetic approaches, the gas−liquid interfacial strategy is beneficial for preparing large-area freestanding cMOF ultrathin films with a controllable thickness at the nanoscale, which is widely employed in materials science and device physics.[8,11,19] However, due to the limitation of intrinsic properties, the pristine cMOF ultrathin film is not capable of the complicated demands in practical applications.[22]

As a kind of significant but complicated application, the photocatalytic CO_2 reduction reaction (CO_2RR) can convert solar energy to chemical fuels, and the whole process involves light absorption, generation, and separation of photogenerated carriers, CO_2 reduction, and H_2O oxidation.[23] Owing to the periodical channel structure and electrical conductivity, cMOFs are capable of optimizing the delivery of substrate molecules and separation of photogenerated electrons and

Received: December 12, 2023
Revised: February 13, 2024
Accepted: February 16, 2024
Published: March 1, 2024

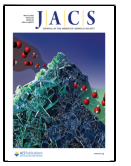

https://doi.org/10.1021/jacs.3c14036
J. Am. Chem. Soc. 2024, 146, 6893−6904

Scheme 1. (a) Different Kinds of Particulate MOF-Based Composites. (b) Schematic Diagrams of [DMC@MOF]-PVK Composite Films and the Perspective View of the Heterostructure and the Catalytic Mechanism for Photocatalytic CO_2RR

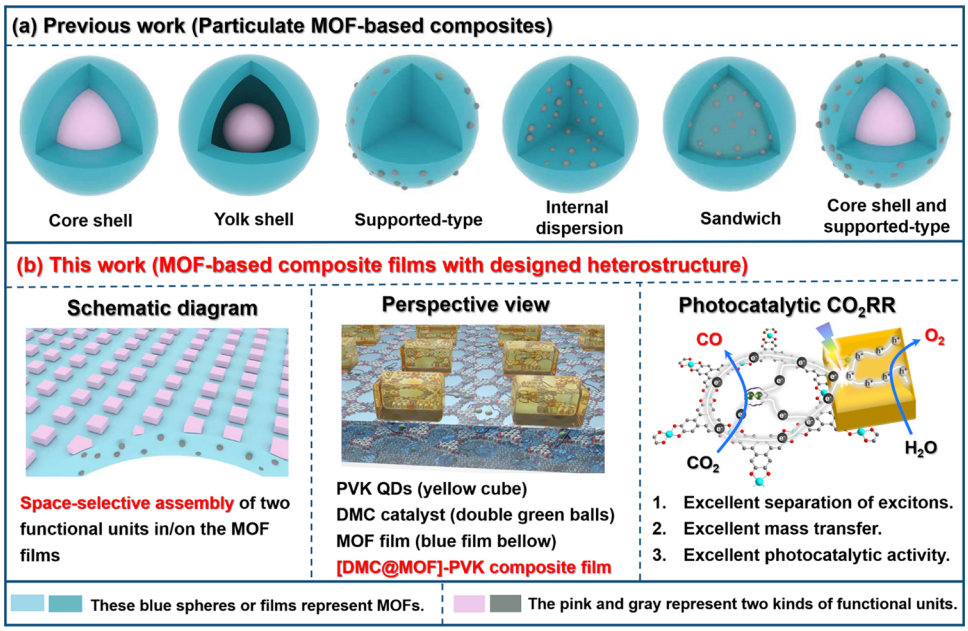

holes. Nevertheless, pure cMOF lacks effective catalytic sites, and the narrow band gap leads to severe electron−hole recombination, which seriously obstructs its development in photocatalysis.[14,24,25] To address these dilemmas, highly effective catalytic sites and photosensitizers should be incorporated into a cMOF. Usually, the random distribution of catalytic sites and photosensitizers in a cMOF is unfavorable for the separation of photogenerated charges. Only when these functional units are controllably immobilized in the appropriate positions of the cMOF, can the long-distance separation of photogenerated electrons and holes be constructed for efficient photocatalysis.[26] However, it is still a huge challenge to realize the controllable assembly of functional units in cMOF ultrathin films, and the corresponding research is still in the blank stage.

Fortunately, particulate MOF-based composite nanomaterials have been studied for a long time.[27] Given the organic−inorganic hybrid characteristics, MOF possesses excellent compatibility with traditional organic (molecules, polymers, *etc.*) and inorganic (metal nanoparticles, clusters, *etc.*) materials, which promises the construction of diverse MOF-based composites.[27] As shown in Scheme 1a, various heterostructures have been reported, such as the core−shell, yolk−shell, supported type, sandwich structure, and so on.[28−32] However, in practical conditions, the particulate photocatalysts still face several dilemmas in synthesis, catalytic system, and recycling process (*i.e.*, the lab-scale preparation, strict synthetic condition, light scattering of suspension and so on).[33−36] By contrast, as a burgeoning subject, the ultrathin film catalyst possesses unique advantages in comparison with the particulate counterpart, as shown in Scheme S1. (1) Large-scale preparation and mechanical processing is more feasible for films.[33] (2) The transmission of light in a uniform ultrathin film is better than that in a suspension solution containing particulates.[34,35] (3) The thickness of the film is much easier to regulate than the morphology of nanomaterials.[19,30] (4) The recycling of the film catalyst is simpler than that of particulate samples.[36] Hence, a large number of ultrathin film samples have been designed and prepared for various fields. Based on the above-mentioned facts, not only in academic fields but also in practical applications, it is of huge significance to develop a reliable synthesis strategy for cMOF-based composite ultrathin film photocatalysts.

In this work, we employed the steric effect and electrostatic interaction to realize the space-selective assembly of molecular catalysts and photosensitizers in cMOF ultrathin films for the photocatalytic CO_2RR with H_2O as an electron donor. First, copper catecholate (Cu-CAT) composed of Cu ions and HHTP (HHTP = 2,3,6,7,10,11-hexahydroxytriphenylene) was selected as a cMOF.[37] The large-area Cu-CAT ultrathin film was prepared on an aqueous surface and then transferred onto a quartz substrate. Then, the dinuclear-metal molecular catalysts (DMC) and perovskite (PVK) quantum dots (QDs) as photosensitizers were integrated into a Cu-CAT film.[38,39] Based on the synergistic effect of steric effects and electrostatic interaction, electropositive DMC was injected into the anionic channels of Cu-CAT, and electronegative PVK was immobilized on the electropositive film surface. The as-prepared [DMC@Cu-CAT]-PVK film controllably integrated catalytic centers and photosensitive centers. The space-selective distribution of DMC and PVK in/on the Cu-CAT ultrathin film was clearly characterized by a series of electron microscopies. In the photocatalytic CO_2RR with H_2O as an electron donor, the as-prepared [DMC@Cu-CAT]-PVK composite films exhibited excellent activity, and the highest CO yield reached 133.36 $\mu mol \cdot g^{-1} \cdot h^{-1}$, which was much higher than that of PVK or DMC-PVK. Based on the control experiment and *in situ* characterization results, the space-selective assembly of DMC and PVK realized the long-distance separation of photogenerated charges, and the electronically active Cu-CAT as a conductive channel facilitated the charge transfer from PVK to DMC, which improved the separation efficiency of photogenerated electrons and holes. Moreover, the lateral dimension of the as-prepared Cu-CAT ultrathin film reached the wafer scale, and the as-prepared film could be tailored into small pieces with desired sizes. These small pieces

https://doi.org/10.1021/jacs.3c14036
J. Am. Chem. Soc. 2024, 146, 6893−6904

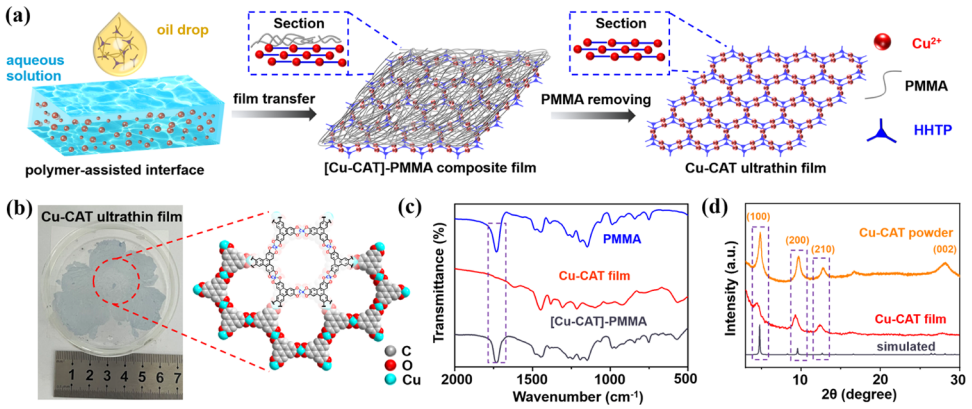

Figure 1. (a) Scheme of the fabricating Cu-CAT ultrathin film via the polymer-assisted gas−liquid interface strategy. (b) Optical photo and the crystal structure of the Cu-CAT film. (c) FTIR spectra of PMMA, Cu-CAT, and [Cu-CAT]-PMMA films. (d) XRD profiles of the simulated one, Cu-CAT film, and Cu-CAT powder sample.

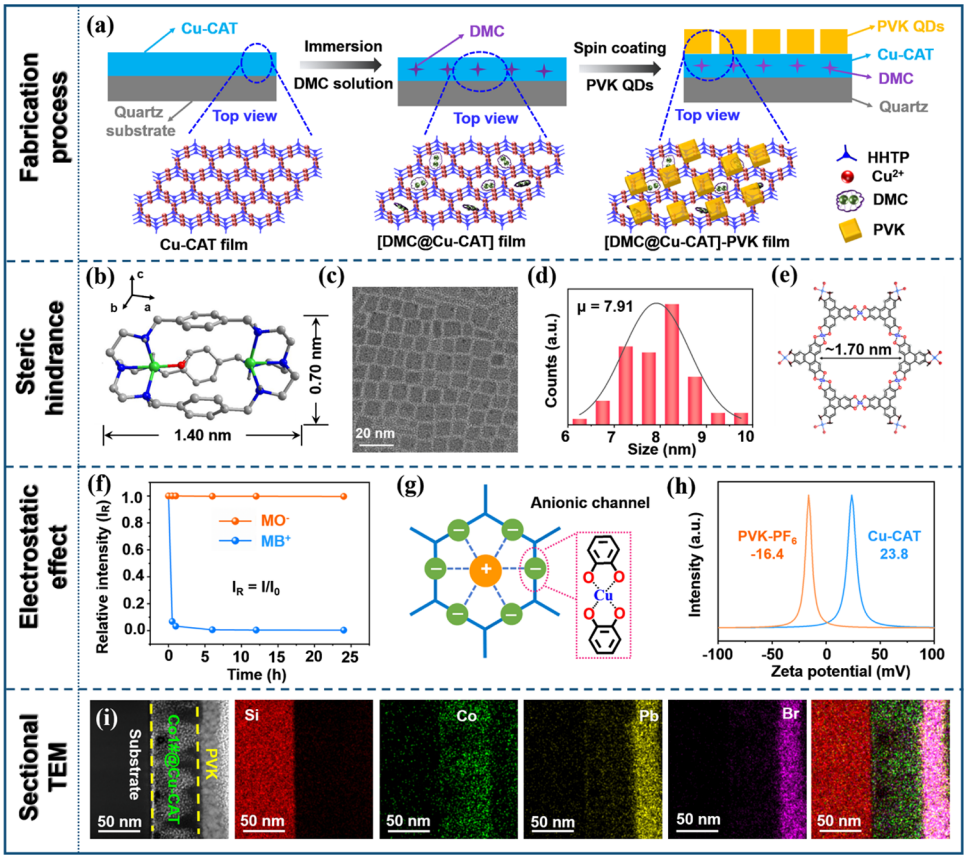

Figure 2. (a) Fabricating process of the [DMC@Cu-CAT]-PVK composite film. (b) Molecular structure and size of Co1# DMC. The gray, blue, green, red, and dark gray balls represent carbon, nitrogen, cobalt, oxygen, and hydrogen atoms, respectively. (c) TEM image of PVK−PF_6 QDs. (d) Diameter histogram of PVK−PF_6 QDs. (e) Pore size of Cu-CAT. (f) Relative intensities (I_R) of the MB^+ characteristic peak at 662.5 nm and the MO^- characteristic peak at 464.5 nm in the time-dependent UV−vis spectra of dye adsorption experiments with Cu-CAT. (g) Schematic diagram of the anionic channel of Cu-CAT. (h) Zeta potentials of PVK−PF_6 and Cu-CAT in ethyl acetate. (i) Sectional TEM image and the corresponding elemental mapping images of the [DMC@Cu-CAT]-PVK composite film.

were integrated into one device as a multilayer film photocatalyst. In the light-enriching reactor, the CO area yield for 10-layer films reached 1115.92 $\mu mol^{-1} \cdot m^{-2}$ in 4 h. To our knowledge, [DMC@Cu-CAT]-PVK is the first example of a cMOF ultrathin film with space-selective assembly of two exotic functional materials, which boosts the development of MOF-based films and highlights the ultrathin film photocatalysts for CO_2RR.

RESULTS AND DISCUSSION

Preparation and Characterization of Cu-CAT Ultrathin Films. Based on previous reports, Cu-CAT possesses excellent electrical conductivity and can be prepared at room temperature.[11] Hence, Cu-CAT was selected to fabricate cMOF ultrathin films. *Via* the polymer-assisted strategy, an oil solution containing poly(methyl methacrylate) (PMMA) and HHTP was dropped onto the surface of a cupric acetate

https://doi.org/10.1021/jacs.3c14036
J. Am. Chem. Soc. 2024, 146, 6893−6904

aqueous solution. After 24 h, a light blue film, [Cu-CAT]-PMMA, was synthesized on the aqueous surface (Figures 1a and S1). For intactly transferring as-prepared [Cu-CAT]-PMMA films onto a quartz substrate, the surface of the substrate should be hydrophilic to minimize the deformation of as-prepared films during the transferring process. Therefore, the surface of the substrate was treated with oxygen plasma and a piranha solution. The contact angle measurements showed that the water drop was spread on the hydroxyl group (−OH)-decorated substrate (Figures S2 and S3 and Video 1). Hence, the abundant −OH guaranteed the hydrophilic property of the substrate, which was crucial for the transfer of the intact Cu-CAT film. As for the [Cu-CAT]-PMMA film on the substrate, the PMMA top layer was removed via an immersing process in an anisole solution, and the pure Cu-CAT film was retained on the quartz substrate (Figure 1a,b). As shown in Figure S4, the optical microscopy (OM) images of [Cu-CAT]-PMMA and Cu-CAT showed that the film color changed from green to blue, and the oleaginous layer disappeared, which preliminarily indicated the removal of PMMA. Moreover, in FTIR spectra (Figures 1c and S5), the characteristic peak of $\nu_{c=o}$ at 1730 cm^{-1} of PMMA disappeared in Cu-CAT films, which further confirmed the release of the PMMA layer. After PMMA was released, both the OM and scanning electron microscopy (SEM) images showed that the integrity was still maintained (Figures S4 and S6), although the surface roughness (R_q) increased from 1.0 to 13.6 nm (Figure S7). Based on the atomic force microscopy (AFM) result (Figure S8), the average thickness of the as-prepared Cu-CAT film was around 59.71 nm. To reveal the crystalline structure, film X-ray diffraction (XRD) was conducted on 10 layers of the Cu-CAT film sample, and the characterized peaks at 4.9, 9.5, 12.6, and 27.5° corresponded to the (100), (200), (210), and (002) crystal faces, respectively,[40] which were maintained with those of the simulated one and powder sample (Figure 1d). As shown in Figure S9, the TEM and SEM images of the Cu-CAT powder sample revealed the nanorod morphology. Besides, the UV−vis spectrum of the as-prepared film was also consistent with the previous report, and Cu-CAT exhibited the capacity to absorb near-infrared light (Figures S10 and S11).[40]

In order to measure the electronic conductivity of the films, gold interdigital electrodes were deposited on Cu-CAT films to construct a two-terminal device, as shown in Figure S12. The $I-V$ measurement results showed that the average conductivity reached 0.13 S/m (Figure S13). Based on these results, an ultrathin, crystalline, and conductive Cu-CAT film was successfully prepared and transferred onto quartz substrates for further employment. In context, the Cu-CAT ultrathin film was named as a Cu-CAT film for concision.

Preparation and Characterization of [DMC@Cu-CAT]-PVK Composite Films. For pursuing superior performance, it is a feasible and reliable approach to design and construct heterostructures for cMOF-based composite films. In photocatalysis, efficient catalytic sites and photosensitizers were two important components that should be introduced into a cMOF, and only the controllable assembly of these functional units could facilitate the separation of photogenerated electrons and holes to the maximum extent (Figure 2a). Among numerous catalysts, molecular catalysts with a clear structure and catalytic mechanism have been studied for a long time.[41] Especially, the dinuclear-metal complex with the synergistic effect of dual metal sites possesses superior catalytic activity.[42] Hence, three kinds of dinuclear-metal catalysts (DMCs) were prepared and labeled Co1#, Co2#, and Co3# (Figures 2b, S14 and S15). The three kinds of DMC catalysts were prepared based on previous publications, and the FTIR spectra were consistent with the previously reported results, verifying their successful synthesis (Figure S16).[43−45]

As another important component, the photosensitizer acts as the center of light capture to generate photoexcited electrons and holes. $CsPbBr_3$ QDs, as one of the halide perovskite materials, possess excellent light absorption and a long lifetime of photogenerated carriers.[39] Besides, PVK is capable of oxidizing H_2O to O_2 and hence is regarded as an appropriate candidate for photocatalytic CO_2RR.[46] The oleylamine-decorated $CsPbBr_3$ ($CsPbBr_3$−OA) QDs were prepared via a solvothermal approach, and the transmission electron microscopy (TEM) image showed that the average diameter was about 7.97 nm (Figure S17). Ammonium hexafluorophosphate (PF_6^-) was employed to exchange the original OA ligands to prepare $CsPbBr_3$−PF_6 QDs. As shown in the FTIR spectrum of PVK−PF_6 (Figure S18), the characteristic peak of PF_6^- at 835 cm^{-1} demonstrated that OA on the surface of $CsPbBr_3$ was successfully exchanged by PF_6^-.[47] The TEM elemental mapping of $CsPbBr_3$−PF_6 showed the uniform distribution of P, F, Cs, Pb, and Br elements, which further revealed that the surface of PVK was decorated by PF_6^- (Figure S19). The morphology of $CsPbBr_3$−PF_6 QDs was still the nanocube with an average diameter of 7.91 nm, indicating the maintained morphology of $CsPbBr_3$ QDs (Figure 2c,2d). As shown in Figures S20 and S21, the high-resolution transmission electron microscopy (HRTEM) images showed that the lattice spacing of $CsPbBr_3$−OA and $CsPbBr_3$−PF_6 were both 0.58 nm, and the XRD results were also consistent with the previous report (Figure S22),[11] which both demonstrated the maintained crystalline structure of as-prepared $CsPbBr_3$−PF_6. The UV−vis spectrum of $CsPbBr_3$−OA was consistent with that of $CsPbBr_3$−PF_6, indicating the maintained capacity of light capturing (Figure S23). In this context, $CsPbBr_3$−PF_6 was labeled as PVK for concision.

Based on the above-mentioned facts, the as-prepared DMC and PVK were selected to incorporate into Cu-CAT films. In the heterostructure of composite films, conductive Cu-CAT is expected to act as a channel to facilitate the charge transfer between DMC and PVK for a higher separation efficiency of photogenerated electrons and holes. For this purpose, it is crucial to realize the space-selective assembly of these two exotic components in Cu-CAT films. As shown in Figure 2a, the Cu-CAT film was first soaked in a DMC solution, and then PVK was deposited on the surface by spin-coating. It was expected that DMC would be incorporated into the channel of Cu-CAT, and PVK QDs were immobilized on the surface of the films.

During the fabrication process, we hope to realize the space-selective assembly of DMC and PVK by the steric effect and electrostatic interaction. In order to study the steric effect, the pore size of Cu-CAT, the molecular size of DMC, and the diameter of PVK QDs should be precisely characterized. The results of gas adsorption showed that the specific area of Cu-CAT was about 121.72 $m^2 \cdot g^{-1}$ and the pore size was around 1.70 nm, which made it possible to regulate the distribution of DMC and PVK QDs (Figures 2e and S24). As shown in Table S1, the molecular sizes of DMCs were all smaller than 1.70 nm, which allowed DMCs to enter into channels of Cu-CAT. However, the 7.91 nm diameter of the PVK QD was much larger than the pore size of Cu-CAT and hence the steric effect

https://doi.org/10.1021/jacs.3c14036
J. Am. Chem. Soc. 2024, 146, 6893−6904

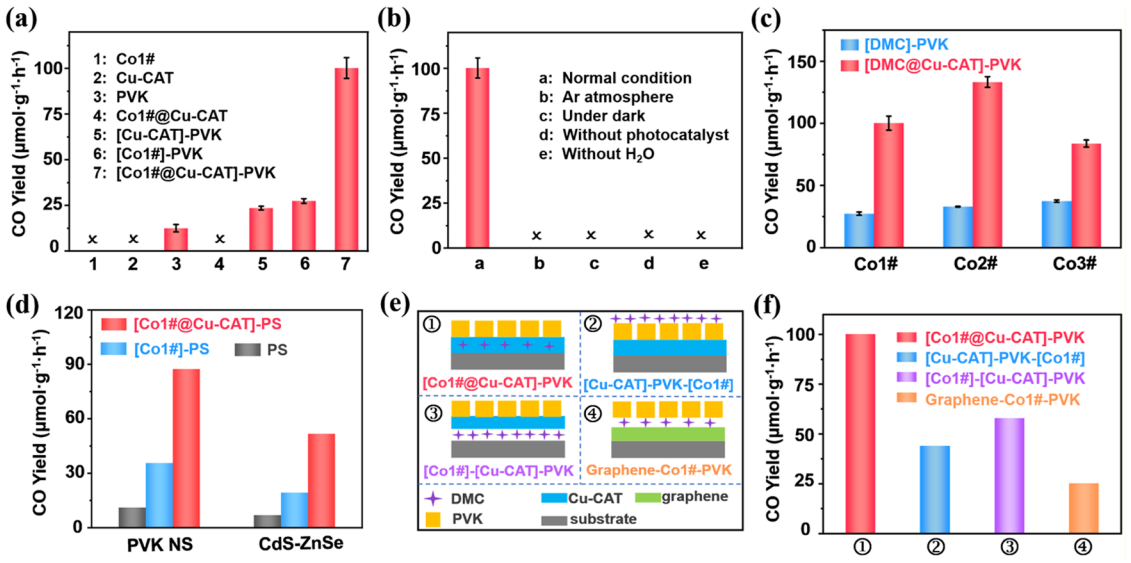

Figure 3. (a) Photocatalytic CO_2RR performance of [Co1#@Cu-CAT]-PVK and control experiments. (b) Control experiments of photocatalytic CO_2RR for [Co1#@Cu-CAT]-PVK. (c) Photocatalytic performance of three kinds of [DMC@Cu-CAT]-PVK films. (d) Photocatalytic performances of PS, [Co1#]-PS, and [DMC@Cu-CAT]-PS film photocatalysts. PVK NS and CdS-ZnSe nanorods were employed as the two kinds of PS to construct film photocatalysts for the CO_2RR. (e) Four types of film photocatalysts for the CO_2RR and (f) corresponding photocatalytic CO_2RR performance.

guaranteed that PVK QDs could not be incorporated into the channels of Cu-CAT.

Moreover, the electrostatic interaction is another important factor in regulating the assembling process. For revealing the electrostatic property of Cu-CAT channels, electropositive methylene blue (MB^+) and electronegative methyl orange (MO^-) were selected for the dye adsorption experiments. Only MB^+ dye could be removed from the aqueous solution by Cu-CAT (Figures 2f, S25, S26, Tables S2 and S3), revealing that the channel of the Cu-CAT film was anionic (Figure 2g). Besides, the as-prepared Cu-CAT film also possessed an adsorbing capacity for MB^+ (Figure S27). Hence, the electropositive DMC could also be introduced into the anionic channel driven by the electrostatic interaction, which was further confirmed by the smaller specific area and pore size of Co1#@Cu-CAT compared to those of Cu-CAT (Figure S28). After incorporation of DMC, the electrical conductivity of [Co1#@Cu-CAT] should be further characterized. The $I-V$ measurement results showed that the average value of electrical conductivity was 0.10 S/m at room temperature (Figure S29), which was a little lower than that of Cu-CAT (0.13 S/m). As for the spin-coating process of PVK QD, the uniform dispersion of PVK QDs was heavily dependent on the wetting property of the Cu-CAT film surface. In the contact angle measurements, the contact angle of water on the Cu-CAT film was about 52.5° (Figure S30), while the ethyl acetate (EA) drop could be totally spread (Video 2), indicating that PVK QDs in EA solution could be uniformly dispersed on the surface of Cu-CAT films. Furthermore, the zeta potential (ζ) of Cu-CAT in EA was −16.4 mV, which was reversed with that of the PVK QD (23.8 mV), as shown in Figure 2h. Hence, the opposite surface charge guaranteed that PVK QDs were effectively assembled on the surface of the Cu-CAT film. Based on these results, it was possible to realize the space-selective assembly of DMC and PVK QDs in the Cu-CAT films.

To clearly reveal the heterostructure, AFM, SEM, and TEM were employed to characterize the composite films. As shown in AFM and SEM images of [Co1#@Cu-CAT] films, the surface roughness just increased a little, and the surface was still intact (Figures S31 and S32). The SEM elemental mapping results of [Co1#@Cu-CAT] showed that the Co and Cu elements were uniformly dispersed in the film, preliminarily revealing that the dinuclear-Co complex was incorporated into Cu-CAT films (Figure S33). As shown in the TEM images of Cu-CAT and [Cu-CAT]-PVK, the nanocubes were uniformly dispersed on the films, and the results of SEM elemental mapping also showed the uniform dispersion of Pb, Cs, and Cu elements (Figures S34−S36), which both confirmed the uniform dispersion of PVK QDs. As for [Co1#@Cu-CAT]-PVK films, the OM images showed that the film color changed from blue to yellow (Figure S37), meaning that the thickness of the film was increased. It was also preliminarily indicated that the surface roughness of [Co1#@Cu-CAT]-PVK was intensified in comparison with that of [Co1#@Cu-CAT]. Following, the AFM image of [Co1#@Cu-CAT]-PVK showed that the R_q value further increased to 23.2 nm (Figure S38), and the SEM image revealed the integrity of films (Figure S39). The SEM elemental mapping results of [Co1#@Cu-CAT]-PVK showed that the Co, Cu, P, and other elements were uniformly dispersed in the lateral dimension of films (Figure S40). For clearly characterizing the layer structure of films in the vertical direction, the cross-sectional TEM images of [Co1#@Cu-CAT]-PVK clearly showed the dual-layer structure of Cu-CAT and PVK (Figure S41). Based on the results of elemental mapping (Figure 2i), the Co element was dispersed in the Cu-CAT layer, but Pb only appeared in the top layer, which convincingly demonstrated that the DMC was incorporated into the channels of Cu-CAT, and PVK was immobilized on the film surface. These results illustrated that the expected [Co1#@Cu-CAT]-PVK composite film was successfully prepared. Based on the above-mentioned facts, via the synergistic effect of steric hindrance and electrostatic interaction, the space-selective assembly of DMC and PVK was

https://doi.org/10.1021/jacs.3c14036
J. Am. Chem. Soc. 2024, 146, 6893−6904

realized in the Cu-CAT film, *i.e.*, the [Co1#@Cu-CAT]-PVK composite film.

Photocatalytic CO_2RR Performance. The as-prepared composite films were employed as photocatalysts for the CO_2RR in the gas−solid photocatalytic system. In a CO_2 atmosphere, a proper amount of water was injected into the catalytic reactor to form vapors under illumination. As shown in Figure 3a, the pure DMC or Cu-CAT film catalyst was not competent to catalyze the CO_2RR with H_2O as an electron donor, but the CO yield of PVK could reach 12.57 $\mu mol \cdot g^{-1} \cdot h^{-1}$, which revealed the necessity of a photosensitizer and the catalytic activity of PVK. As for the PVK-based composite, Co1#-PVK and [Cu-CAT]-PVK exhibited the CO yields of 27.45 and 23.60 $\mu mol \cdot g^{-1} \cdot h^{-1}$, separately, and the catalytic activity was increased by around 2-fold in comparison with that of pure PVK. After space-selective assembly of Co1# and PVK in/on Cu-CAT, the CO yield of the as-prepared [Co1#@Cu-CAT]-PVK composite film increased to 100.29 $\mu mol \cdot g^{-1} \cdot h^{-1}$. In the absence of CO_2 or water vapors, the CO yield of [Co1#@Cu-CAT]-PVK directly decreased to zero (Figure 3b). It was preliminarily demonstrated that CO originated from CO_2, and H_2O might be the electron donor in photocatalytic CO_2RR. Following, the isotope trace experiments demonstrated that the CO product originated from the CO_2 reduction, and the O_2 originated from the H_2O oxidation (Figures S42 and S43). Moreover, the yields of CO and O_2 were 857.89 and 420.42 $\mu mol \cdot g^{-1}$, respectively (Figure S44). The results all demonstrated that the CO and O_2 products were derived from CO_2 and H_2O, respectively. Besides, the results of control experiments also proved that radiation and photocatalysts were necessary for photocatalytic CO_2RR.

In the cyclic reaction experiments (Figure S45), the CO yield gradually decreased from 100.59 to 91.09 to 90.48 $\mu mol \cdot g^{-1} \cdot h^{-1}$. In addition, the [Co1#@Cu-CAT]-PVK film photocatalyst was employed for CO_2RR under solar irradiation, and the CO yields on sunny, cloudy, overcast, and rainy days reached 124.21, 84.95, 66.55, and 23.00 $\mu mol \cdot g^{-1} \cdot h^{-1}$ (Figure S46), respectively. After the photocatalytic reaction, the [Co1#@Cu-CAT]-PVK film was further characterized to verify the morphology and crystal structure of the films. As shown in Figure S47, the TEM images showed that PVK QDs were still anchored on the surface of Cu-CAT, and the obvious lattice fringe was still observed on the surface of PVK QDs. In order to further characterize the crystal structures of Cu-CAT and PVK in the composite film, XRD was employed to characterize the used film photocatalysts. As shown in Figure S48, the characterized peaks at 4.9, 9.5, and 12.6° correspond to the (100), (200), and (210) crystal faces of Cu-CAT, respectively. Moreover, the characterized peaks of the PVK QDs were also maintained. The above-mentioned results demonstrated that the crystal structures of Cu-CAT and PVK QDs could both be maintained after photocatalysis. Based on the ESR spectra, the concentration of the Br vacancy remained almost constant during photocatalysis (Figure S49).

As an important criterion to evaluate the synthetic strategy, the universality of constructing an MOF-based composite film photocatalyst should be further discussed and studied. *Via* the same synthetic approach, Co2# and Co3# DMCs could also be introduced into the Cu-CAT film together with PVK. The as-prepared [Co2#@Cu-CAT]-PVK and [Co3#@Cu-CAT]-PVK also possessed superior photocatalytic CO_2RR activity than [Co2#]-PVK and [Co3#]-PVK samples (Figure 3c), respectively. In addition, PVK as the photosensitizer (PS) component should also be exchanged by other kinds of semiconductor photocatalysts, which should possess the capacity for visible-light absorption and catalysis of water oxidation. Hence, two kinds of photocatalysts (*e.g.*, $CsPbBr_3$ nanosheet and CdS/ZnSe nanorod) were selected to prepare and employed in this strategy. TEM, XRD, UV−vis spectroscopy, and other characterizations demonstrated the successful preparation of the $CsPbBr_3$ nanosheet (abbreviated as PVK NS) and the CdS/ZnSe nanorod (Figures S50−S57). The corresponding details are listed in the Supporting Information. *Via* a similar approach, [Co1#Cu-CAT]-[PVK NS] and [Co1#@Cu-CAT]-[CdS/ZnSe] film photocatalysts were successfully prepared and then employed in photocatalytic CO_2RR. As shown in Figure 3d, the CO yields of PVK NS, [Co1#]-[PVK NS], and [Co1#@Cu-CAT]-[PVK NS] reached 11.14, 35.57, and 87.41 $\mu mol \cdot g^{-1} \cdot h^{-1}$ CO yields, respectively. Similarly, [Co1#@Cu-CAT]-[CdS/ZnSe] also showed the highest CO yield (51.83 $\mu mol \cdot g^{-1} \cdot h^{-1}$) compared with those of [Co1#]-[CdS/ZnSe] (19.32 $\mu mol \cdot g^{-1} \cdot h^{-1}$) and CdS/ZnSe (7.04 $\mu mol \cdot g^{-1} \cdot h^{-1}$). Hence, the introduction of Cu-CAT greatly increased the performance of photocatalytic CO_2RR. These observations all demonstrated that the space-selective assembly of DMCs and PS in/on cMOFs realized the controllable integration of the catalytic center and the photosensitizer, which is a universal strategy to prepare efficient photocatalysts for CO_2 reduction.

Photocatalytic Mechanism. For revealing the mechanism of photocatalytic CO_2RR by the composite films, in situ FTIR measurement was employed to detect the intermediates. As shown in Figure S58, the characteristic peak of *COOH at 1637 cm^{-1} was clearly observed, and *CO was detected at 2077 cm^{-1} after 3 min. This result, together with the fact that the *COOH characteristic peak became more and more strong, revealed that the rate-limiting step was the formation of *CO (*COOH + H^+ + e^- → *CO + H_2O).

To reveal the bridge effect of Cu-CAT, Co1# was immobilized on the top of the PVK layer ([Cu-CAT]-PVK-[Co1#]) and below the bottom of the Cu-CAT layer ([Co1#]-[Cu-CAT]-PVK), respectively (Figure 3e). The results of the photocatalytic CO_2RR showed that the corresponding CO yields reached 44.15 and 57.99 $\mu mol \cdot g^{-1} \cdot h^{-1}$, respectively (Figure 3f). These values were lower than that of [DMC@cMOF]-PVK but higher than that of [Co1#]-PVK, meaning that the unique heterostructure was very critical to the excellent photocatalytic activity. Besides, the periodic channel structure of Cu-CAT guaranteed the mass transfer for CO_2 and H_2O molecules, which was also an important factor for the improved catalytic activity of the composite film catalyst. In order to prove this viewpoint, the graphene nanosheets were employed to replace the Cu-CAT film, and the CO yield (25.29 $\mu mol \cdot g^{-1} \cdot h^{-1}$) of the as-prepared graphene-[Co1#]-PVK film catalyst was much lower than that of [Co1#@Cu-CAT]-PVK. Based on these results of control experiments, it could be concluded that the electrical conductivity and periodic channel of the Cu-CAT film were both beneficial for optimizing the photocatalytic performance. At the same time, the unique heterostructure of [DMC@cMOF]-PVK was favorable for facilitating mass delivery and photogenerated charge separation, which was the prerequisite for the excellent photocatalytic performance of the CO_2RR.

The excellent separation of photogenerated electrons and holes was heavily dependent on the route of charge transfer in the heterostructures of photocatalysts. Prior to probing the

https://doi.org/10.1021/jacs.3c14036
J. Am. Chem. Soc. 2024, 146, 6893−6904

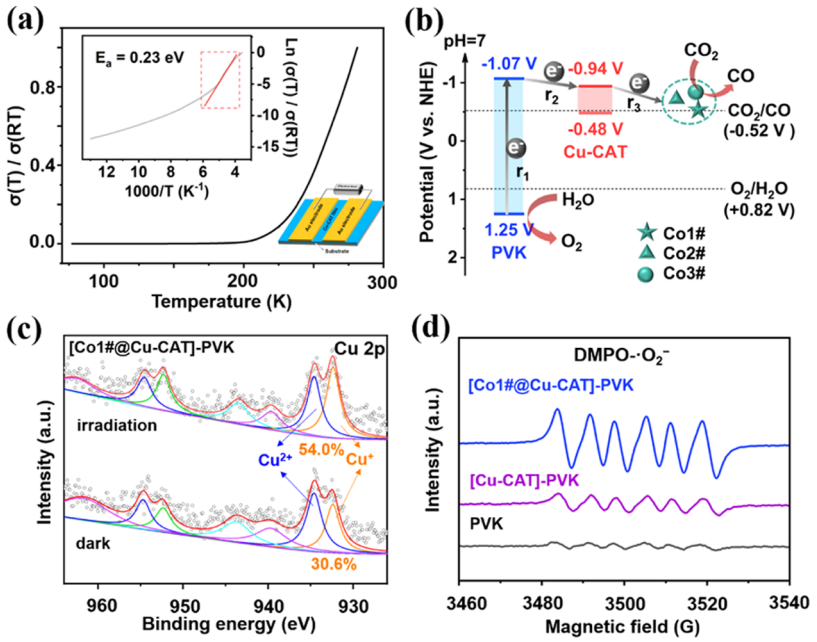

Figure 4. (a) Temperature-dependent conductance of Cu-CAT films. (b) Band alignment of components in [Co1#@Cu-CAT]-PMMA films. (c) High-resolution XPS spectra of Cu 2p for [Co1#@Cu-CAT]-PVK in the dark (bottom line) and under irradiation (top line). (d) ESR spectra of DMPO-$^{\bullet}O_2^-$ in O_2/methanol for PVK (black line), [Cu-CAT]-PVK (purple line), and [Co1#@Cu-CAT]-PVK (blue line).

transfer route of photoexcited charges, the band structures of components in composite films should be first determined. As the conductive bridge between DMC and PVK, the electrical conductivity of the Cu-CAT film reached 0.13 S/m at room temperature (Figure S10). Even after introducing DMC, the electrical conductivity of DMC@Cu-CAT could still remain at 0.10 S/m (Figure S29). As for the conductive MOFs, the temperature-dependent conductivity measurement was much more appropriate to characterize the band gap (E_g) of the Cu-CAT film. The E_g of the semiconductor could be derived from the activation energy (E_a), *i.e.*, $E_g = 2E_a$[1] and hence the E_g of Cu-CAT was estimated to be 0.46 eV (Figures 4a and S59). The Mott−Schottky result revealed that the conduction band was at −0.94 V (Figure S60), and the valence band was calculated as −0.48 V, as shown in Figure 4b. As for the photosensitizer PVK, the Tauc and Mott−Schottky plots determined the conduction band (−1.07 V) and E_g (2.32 eV), respectively, as shown in Figure S61. Then, the cyclic voltammogram (CV) and differential pulse voltammetry (DPV) results of Co1#, Co2#, and Co3# DMC showed that the reductive peaks were at −0.52, −0.88, and −0.87 V, respectively (Figures S62−S64). The energy levels or reductive potentials of these components are all summarized in Figure 4b. In thermodynamics, the PVK could be irradiated to generate excited electrons and holes. The holes were employed to oxidize H_2O on PVK, and then the electrons were transferred via conductive Cu-CAT to DMC for CO_2 reduction.

For directly characterizing the charge transfer, X-ray photoelectron spectroscopy (XPS) was conducted on film catalysts, which could clearly show the detailed interaction behavior between components in the composite film. As depicted in the XPS profile of [Cu-CAT]-PVK (Figure S65), the characteristic peaks of Cs 3d, Br 2p, and Pd 4f binding energy all showed an obvious shift to higher energy in comparison with that of pure PVK. Besides, the percentage of Cu^+ in [Cu-CAT]-PVK also increased from 5.4 to 16.0%, compared with that of Cu-CAT (Figure S65d). These results both indicated that the strong interaction facilitated the electron transfer from the PVK to Cu-CAT film. Similar phenomena occurred in [Co1#@Cu-CAT]-PVK (Figure 4c), which further demonstrated the strong interaction between Cu-CAT and PVK. For further characterizing the electron transfer in photocatalysis, in situ XPS was necessary to confirm the percentage of Cu^+ within composite film catalysts. When [Co1#@Cu-CAT]-PVK was illuminated under light, not only the percentage of Cu^+ further increased from 43.0 to 54.0% (Figure 4c and Table S4) but also there was a positive shift as for binding energy of Br 2p (Figure S66), certifying that photogenerated electrons transferred from PVK to the Cu-CAT film (*i.e.*, the r_2 route in Figure 4b). Due to the limited detection depth of XPS, the binding energy of Co was hardly detected, and it was not proven that the photogenerated electron further transferred from Cu-CAT to Co1#. As for [Co1#]-PVK, the binding energy of Co 2p became lower under irradiation, meaning that the photogenerated electron of PVK could transfer to Co1# (Figure S67). Besides, as for [Co1#@Cu-CAT]-PVK, EPR analysis was employed to detect the spin active $^{\bullet}O_2^-$ species using 5,5-dimethyl-1-pyrroline N-oxide (DMPO) as the trapping agent. As shown in Figure 4d, the DMPO-$^{\bullet}O_2^-$ signal of [Co1#@Cu-CAT]-PVK was the highest; the following is that of [Cu-CAT]-PVK, and PVK exhibited the lowest signal, meaning that the photogenerated electron was finally transferred to Co1# DMC for the reduction reaction. Following, for certifying catalytic sites for CO_2 reduction, Co1# DMC was poisoned by KSCN, which resulted in the deactivation of Co1# DMC. In the photocatalytic CO_2RR (Figure S68), the CO yield of poisoned [Co1#@Cu-CAT]-PVK was only 17.47 μmol·g^{-1}·h^{-1}, which was slightly higher than that of PVK (12.57 μmol·g^{-1}·h^{-1}) but lower than that of [Cu-CAT]-PVK (27.45 μmol·g^{-1}·h^{-1}). Based on these results, the photocatalytic activity of poisoned [Co1#@Cu-CAT]-PVK mainly originated from PVK. Compared with [Co1#@Cu-CAT]-PVK, the activity of poisoned

https://doi.org/10.1021/jacs.3c14036
J. Am. Chem. Soc. 2024, 146, 6893−6904

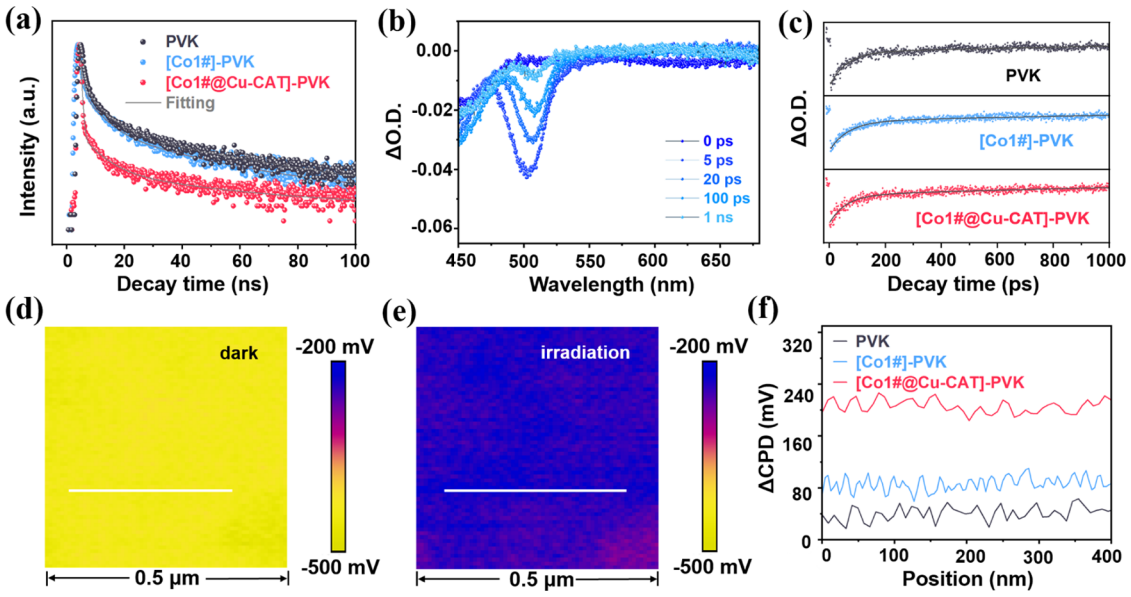

Figure 5. (a) Time-resolved PL decay plots of PVK, [Co1#]-PVK, and [Co1#@Cu-CAT]-PVK. (b) TA spectra recorded of [Co1#@Cu-CAT]-PVK. (c) TA kinetic traces of PVK, [Co1#]-PVK, [Cu-CAT]-PVK, and [Co1#@Cu-CAT]-PVK at 507 nm. The differential SPV images between potential images (d) in the dark and (e) under irradiation. (f) Contact potential difference changes (ΔCPD) in the dark and under the illumination of PVK (black line), [Co1#]-PVK (blue line), and [Co1#@Cu-CAT]-PVK (red line).

[Co1#@Cu-CAT]-PVK was much lower, further revealing the important effect of Co1# DMC in photocatalytic CO_2RR. Hence, these results forcefully proved that the incorporated Co1# DMC indeed acted as the catalytic sites for CO_2RR. In the photocatalytic reactor, the CO_2 concentration was much higher than that of O_2, and Cu-CAT possessed a capacity for adsorbing CO_2 (Figures S69 and S70). Besides, the H_2O oxidation and CO_2 reduction were catalyzed by the PVK layer and DMC incorporated in Cu-CAT (Figure S71), respectively. These results indicated that the concentration of CO_2 around Co sites of DMC was much higher than that of O_2, which avoided the retarding effect of O_2 on CO_2 reduction and guaranteed the proceeding of photocatalytic CO_2RR. Hence, the photogenerated electron on PVK could transfer via conductive Cu-CAT and finally to Co1# DMC for CO_2RR (*i.e.*, the r_3 route in Figure 4b). Based on these results, three routes for charge transfer (r_1, r_2 and r_3) are schemed in Figure 4b.

Owing to the unique routes for charge transfer, the fluorescence intensity of [Co1#@Cu-CAT]-PVK was the lowest compared with those of PVK and [Co1#]-PVK, as shown in the photoluminescence (PL) spectra (Figure S72), proving that the highest separation efficiency of photogenerated carriers was attributed to Cu-CAT. In order to study the charge-transfer dynamics, electrochemical impedance spectroscopy (EIS) and photocurrent measurement were employed to reveal the effect of Cu-CAT on accelerating the charge transfer between PVK and Co1# DMC. The values of the semicircular radius of EIS Nyquist plots for these samples were in a gradually decreased order: PVK > [Co1#]-PVK > [Cu-CAT]-PVK > [Co1#@Cu-CAT]-PVK (Figure S73), revealing that the introduction of Cu-CAT boosted the charge transfer between PVK and Co1# DMC. Moreover, in the photocurrent measurements, the photocurrent of [Co1#]-PVK was slightly higher than that of PVK, but the introduction of Cu-CAT brought a significant increase in photocurrent density (Figure S74), highlighting the important effect of Cu-CAT on facilitating the charge transfer. The highest photocurrent intensity of [Co1#@Cu-CAT]-PVK also signified the best interfacial charge separation. These results remained consistent with those of EIS Nyquist plots, once again indicating the favorable effect of Cu-CAT on the charge transfer from PVK to Co1#.

Furthermore, ultrafast spectrum technologies were employed to characterize the charge-transfer dynamics in depth, which was regarded as a powerful approach to study the mechanism of charge transfer in semiconductors. The time-resolved photoluminescence (TRPL) results showed that the average PL lifetimes of PVK, [Co1#]-PVK, and [Co1#@Cu-CAT]-PVK were 13.5736, 9.8314, and 5.7429 ns, respectively. The accelerated PL decay meant that the conductive Cu-CAT film played an important role in facilitating the charge transfer between PVK and Co1# DMC (Figure 5a and Table S5). Furthermore, in the femtosecond transient absorption (TA) spectra (Figures 5b,c, and S75 and Table S6), the ground-state bleaching (GSB) of PVK was observed as an obvious negative peak at 507 nm. As shown in Figure 5b,c, the intensity at 507 nm was studied at different delay times. [Co1#@Cu-CAT]-PVK possessed the fastest GSB rate (0.83 ns) compared with PVK (1.57 ns) and [Co1#]-PVK (1.01 ns), certifying that Cu-CAT as a conductive layer was beneficial for the charge transfer between PVK and Co1# DMC.

It was well known that the better the charge separation, the more charge was enriched on the surface of the catalysts. The surface potential change under illumination directly reflected the photogenerated charge spatial separation, which could be characterized by surface photovoltage (SPV) by Kelvin probe force microscopy (KPFM). Hence, the magnitude of SPV was employed to characterize the charge density on the surface of catalysts, and the SPV results were obtained by different values between potential images in the dark and light, which was defined as ΔCPD (Figure 5d,e). The ΔCPD of [Co1#@Cu-CAT]-PVK (206 mV) was the highest in comparison with those of PVK (41 mV) and [Co1#]-PVK (86 mV, Figures 5f

https://doi.org/10.1021/jacs.3c14036
J. Am. Chem. Soc. 2024, 146, 6893−6904

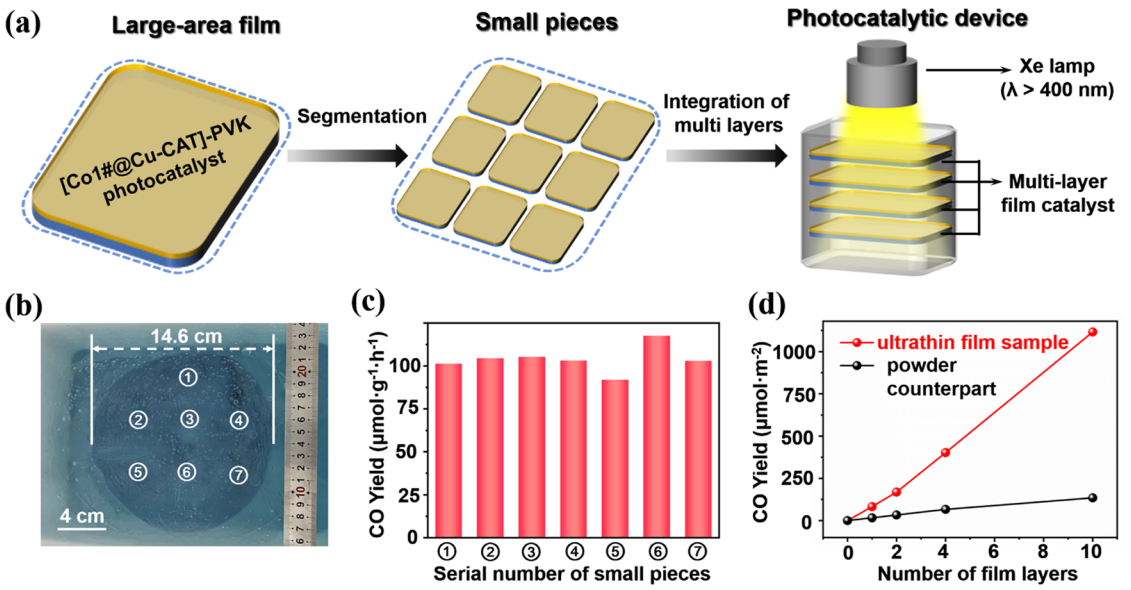

Figure 6. (a) Schematic diagram for mechanical processing on the large-area [Co1#@Cu-CAT]-PVK film (the large-area film was tailored into small pieces, and then multilayers of these pieces were integrated into one device for photocatalysis). (b) As-prepared wafer-scale [Cu-CAT]-PMMA film on the aqueous surface. (c) Photocatalytic CO_2RR performance of [Co1#@Cu-CAT]-PVK film catalysts prepared from the wafer-scale film sample. (d) Photocatalytic CO_2RR performance in 4 h for the multilayer film catalyst device and the powder counterpart.

and S76−S78, Table S7), which signified the highest efficient separation of photogenerated electrons and holes in [Co1#@Cu-CAT]-PVK. The above-mentioned evidence all demonstrated that the best separation efficiency of photogenerated electrons and holes in [Co1#@Cu-CAT]-PVK was attributed to the conductive Cu-CAT and the unique space-selective assembly of DMC and PVK in the heterostructure.

As a universal strategy, the effect of Cu-CAT on facilitating photogenerated charge separation should also be studied in the PVK NS and CdS/ZnSe-based composite film photocatalysts. The energy levels of PVK NS and CdS/ZnSe nanorods were also suitable for charge transfer in [Co1#@Cu-CAT]-PS films (Figures S79−S83), in which the photogenerated electron of PVK NS or CdS/ZnSe could be transferred via Cu-CAT and finally to Co1# DMC. The details have been discussed in the Supporting Information. Similar to [Co1#@Cu-CAT]-PVK, [Co1#@Cu-CAT]-[PVK NS] possessed the highest photocurrent and the smallest values of the semicircular radius of EIS Nyquist plots in comparison with PVK NS and [Co1#]-[PVK NS], as shown in Figure S84. A similar phenomenon also occurred in the [Co1#@Cu-CAT]-[CdS/ZnSe] films (Figure S85), meaning that Cu-CAT played an important role in improving the separation efficiency of photogenerated electrons and holes.

As for the general strategy, the selection criteria of semiconductor PS components were very necessary and should be discussed in detail. (1) The size of the PS component should be large enough to prevent the incorporation into channels of MOFs. (2) The negative surface potential of PS materials is beneficial for their assembly on the surface of Cu-CAT via the electrostatic effect. (3) The PS component should possess the capacity of visible-light absorption. (4) PS components should be capable of catalyzing water oxidation. (5) The proper band structures of PS components are necessary so that the photogenerated electrons can be transferred from PS to Cu-CAT to DMC for CO_2 reduction.

In summary, the conductive Cu-CAT layer is indeed beneficial for the separation of photogenerated carriers, which is attributed to the space-selective assembly of DMC and PS in [Co1#@Cu-CAT]-PS composite films.

Integrated Device of Film Photocatalysts. The large-area MOF-polymer film could be easily fabricated via the polymer-assisted gas/liquid interface strategy, and the excellent mechanical stability of the as-prepared film enables a series of subsequent processing to cater to different demands (Figure 6a). As shown in Figure 6b, the fabricating size of [Cu-CAT]-PMMA reached the wafer scale (14.6 cm diameter). The wafer-scale [Co1#@Cu-CAT]-PVK film photocatalysts could be tailored into small pieces with desired sizes and then integrated into one light-enriching reactor to construct an integrated photocatalysis device, as shown in Figure 6a.

In these batch-prepared film catalysts, the average CO yield of these samples could reach around 103.88 $\mu mol \cdot g^{-1} \cdot h^{-1}$ (Figure 6c), which signified the uniformity of large-area MOF-based films and the reliability of this synthetic strategy. In cycling experiments, the film catalyst still kept excellent catalytic activity without an obvious decrease (Figure S86). Compared with the previously reported PVK-based photocatalysts for the CO_2RR, [Co1#@Cu-CAT]-PVK still exhibits huge superiority in mass activity for the photocatalytic CO_2RR (Table S8 and Figure S87). Hence, this synthetic strategy realized the mass production of photocatalysts with high performance.

In the photocatalytic system, the ultrathin film photocatalyst possessed excellent light transmittance and conquered the light scattering dilemma in comparison to particulate catalysts (Scheme S1). Hence, multilayer film catalysts were arranged in a vertical direction as a photocatalytic device to enhance the light absorption and utilization. Based on the detection of the light intensity meter, the intensity of transmission light decreased along with increasing the number of film layers (Figures S88 and S89). As for 10-layer ultrathin film catalysts, the transmission light intensity was only 10% of the incident light intensity. A similar phenomenon was further confirmed

https://doi.org/10.1021/jacs.3c14036
J. Am. Chem. Soc. 2024, 146, 6893−6904

by UV−vis spectra (Figure S90). The abundant visible light could be transmitted through the multilayer films, which was absorbed by PVK QDs. Then, the multilayer film catalyst was placed in the light-enriching device (Figures S91 and S92), and each layer of film catalysts could be illuminated to the maximum extent. Along with increasing the layer number, the area activity gradually increased, and the 10-layer film catalyst showed a 1115.92 μmol·m^{-2} CO yield in 4 h (Figure 6d).

To reveal the superiority of the multilayer film photocatalyst, the powder counterpart sample with the equivalent amount of Co1#, Cu-CAT, and PVK in the film sample was also dropped onto a quartz substrate. As for the 10-layer film photocatalyst, the area activity of the powder counterpart sample (134.40 μmol·m^{-2} CO yield) was much lower than that of the film sample (Figure 6d). The low photocatalytic activity of powder could be ascribed to the ambiguous heterostructure and low light transmission of powder counterpart samples. In addition, the mass activities of [Co1#]-PVK, [Cu-CAT]-PVK, and [Co1#@Cu-CAT]-PVK powder samples were 15.14, 12.67, and 20.23 μmol·g^{-1}·h^{-1} CO yields (Figure S93), respectively, which were all lower than the film counterparts. Hence, these results further verified the necessity of developing film photocatalysts. Based on the above-mentioned facts, not only did the synthetic strategy realize large-area preparation of film photocatalysts with specific heterostructures but also film samples could be easily integrated into one device to improve the photocatalytic area activity for CO_2RR. Hence, this work greatly boosts the practical application of MOF-based films and provides a novel avenue for photocatalysis.

CONCLUSIONS

In this work, we employed the synergistic effect of steric hindrance and electrostatic attraction to fabricate [DMC@Cu-CAT]-PVK ultrathin composite films, in which the DMC and PVK were integrated into the channel and on the surface of the Cu-CAT film, respectively. In this unique heterostructure, Cu-CAT possessed a periodic channel structure and excellent electrical conductivity, which guaranteed mass and charge transfer during photocatalysis. Hence, [DMC@Cu-CAT]-PVK exhibited superior activity for photocatalytic CO_2RR, which was attributed to the space-selective assembly of DMC and PVK. Furthermore, we successfully realized the wafer-scale fabrication of a Cu-CAT-based film photocatalyst, which laid a foundation for mass production of film catalysts. Owing to the good machinability of the film, multiple layers of the film catalyst could be assembled into one integrated device, and the area activity for the CO_2RR was greatly improved to 1115.92 μmol·m^{-2} CO yield in 4 h, which was much higher than that of the powder counterpart. The exploration of the fabrication and photocatalysis of film samples not only boosts the development of MOF-based composites but also paves a novel avenue for future photocatalysts.

ASSOCIATED CONTENT

Supporting Information

The Supporting Information is available free of charge at https://pubs.acs.org/doi/10.1021/jacs.3c14036.

Details about characterization, reagents, additional synthesis methods, and supporting information figures and tables (PDF)

Transfer process of the MOF-PMMA film from the aqueous surface onto the −OH-decorated quartz substrate (AVI)

Contact angle of the water drop on Cu-CAT films (AVI)

AUTHOR INFORMATION

Corresponding Authors

Kuo Yuan − *Institute for New Energy Materials and Low Carbon Technologies, School of Materials Science & Engineering, Tianjin University of Technology, Tianjin 300384, China; Department of Chemistry, School of Science & Key Laboratory of Organic Integrated Circuits, Ministry of Education, Tianjin University, Tianjin 300072, China; Key Laboratory of Advanced Energy Materials Chemistry (Ministry of Education), Nankai University, Tianjin 300071, China;* orcid.org/0000-0002-4097-135X; Email: yuankuo@email.tjut.edu.cn

Dichang Zhong − *Institute for New Energy Materials and Low Carbon Technologies, School of Materials Science & Engineering, Tianjin University of Technology, Tianjin 300384, China*; Email: dczhong@email.tjut.edu.cn

Tong-Bu Lu − *Institute for New Energy Materials and Low Carbon Technologies, School of Materials Science & Engineering, Tianjin University of Technology, Tianjin 300384, China;* orcid.org/0000-0002-6087-4880; Email: lutongbu@tjut.edu.cn

Wenping Hu − *Department of Chemistry, School of Science & Key Laboratory of Organic Integrated Circuits, Ministry of Education, Tianjin University, Tianjin 300072, China; Joint School of National University of Singapore and Tianjin University, International Campus of Tianjin University, Binhai New City, Fuzhou 350207, China;* orcid.org/0000-0001-5686-2740; Email: huwp@tju.edu.cn

Authors

Keying Tao − *Institute for New Energy Materials and Low Carbon Technologies, School of Materials Science & Engineering, Tianjin University of Technology, Tianjin 300384, China*

Tianqun Song − *Institute for New Energy Materials and Low Carbon Technologies, School of Materials Science & Engineering, Tianjin University of Technology, Tianjin 300384, China; Department of Chemistry, School of Science & Key Laboratory of Organic Integrated Circuits, Ministry of Education, Tianjin University, Tianjin 300072, China; Key Laboratory of Advanced Energy Materials Chemistry (Ministry of Education), Nankai University, Tianjin 300071, China*

Ying Zhang − *Institute for New Energy Materials and Low Carbon Technologies, School of Materials Science & Engineering, Tianjin University of Technology, Tianjin 300384, China*

Tao Zhang − *Wuhan National High Magnetic Field Center and School of Physics, Huazhong University of Science and Technology, Wuhan 430074, China*

Fei Wang − *CAS Key Laboratory of Nanosystem and Hierarchical Fabrication, National Center for Nanoscience and Technology, Beijing 100190, China*

Shuming Duan − *Department of Chemistry, School of Science & Key Laboratory of Organic Integrated Circuits, Ministry of Education, Tianjin University, Tianjin 300072, China; Joint School of National University of Singapore and Tianjin*

https://doi.org/10.1021/jacs.3c14036
J. Am. Chem. Soc. 2024, 146, 6893−6904

University, International Campus of Tianjin University, Binhai New City, Fuzhou 350207, China

Zheng Chen − *Department of Chemistry, School of Science & Key Laboratory of Organic Integrated Circuits, Ministry of Education, Tianjin University, Tianjin 300072, China*

Lujiang Li − *Key Laboratory of Advanced Energy Materials Chemistry (Ministry of Education), Nankai University, Tianjin 300071, China;* orcid.org/0000-0003-1579-3739

Xiaotao Zhang − *Department of Chemistry, School of Science & Key Laboratory of Organic Integrated Circuits, Ministry of Education, Tianjin University, Tianjin 300072, China*

Zhiyong Tang − *CAS Key Laboratory of Nanosystem and Hierarchical Fabrication, National Center for Nanoscience and Technology, Beijing 100190, China;* orcid.org/0000-0003-0610-0064

Complete contact information is available at: https://pubs.acs.org/10.1021/jacs.3c14036

Author Contributions

[▽]K.Y., K.T., and T.S. contributed equally to this work.

Funding

This work was supported by the National Key Research and Development Program of China (2022YFA1502902, 2022YFB3603800), the National Natural Science Foundation of China (22205162, 22271218, 21931007, 22001043, 22071182), the National Natural Science Foundation of China (52121002, 51733004, 51725304, 21875158, U21A6002), and the Tianjin Natural Science Foundation (20JCJQJC00300).

Notes

The authors declare no competing financial interest.

■ ACKNOWLEDGMENTS

The authors thank Zongyang Liu and Qisheng Sun for their kind suggestions in writing.

■ REFERENCES

(1) Sun, L.; Campbell, M. G.; Dincă, M. Electrically Conductive Porous Metal-Organic Frameworks. *Angew. Chem., Int. Ed.* **2016**, *55*, 3566−3579.

(2) Wang, Q.; Astruc, D. State of the Art and Prospects in Metal-Organic Framework (MOF)-Based and MOF-Derived Nanocatalysis. *Chem. Rev.* **2020**, *120*, 1438−1511.

(3) Qian, Q.; Asinger, P. A.; Lee, M. J.; Han, G.; Rodriguez, K. M.; Lin, S.; Benedetti, F. M.; Wu, A. X.; Chi, W. S.; Smith, Z. P. MOF-Based Membranes for Gas Separations. *Chem. Rev.* **2020**, *120*, 8161−8266.

(4) Getman, R. B.; Bae, Y. S.; Wilmer, C. E.; Snurr, R. Q. Review and Analysis of Molecular Simulations of Methane, Hydrogen, and Acetylene Storage in Metal-Organic Frameworks. *Chem. Rev.* **2012**, *112*, 703−723.

(5) Allendorf, M. D.; Bauer, C. A.; Bhakta, R. K.; Houk, R. J. T. Luminescent Metal-Organic Frameworks. *Chem. Soc. Rev.* **2009**, *38*, 1330−1352.

(6) Furukawa, H.; Cordova, K. E.; O'Keeffe, M.; Yaghi, O. M. The Chemistry and Applications of Metal-Organic Frameworks. *Science* **2013**, *341*, No. 1230444.

(7) Liu, J.; Goetjen, T. A.; Wang, Q.; Knapp, J. G.; Wasson, M. C.; Yang, Y.; Syed, Z. H.; Delferro, M.; Notestein, J. M.; Farha, O. K.; Hupp, J. T. MOF-Enabled Confinement and Related Effects for Chemical Catalyst Presentation and Utilization. *Chem. Soc. Rev.* **2022**, *51*, 1045−1097.

(8) Wu, G.; Huang, J.; Zhang, Y.; He, J.; Xu, G. Porous Field-Effect Transistros Based on a Semiconductive Metal-Organic Framework. *J. Am. Chem. Soc.* **2017**, *139*, 1360−1363, DOI: 10.1021/jacs.6b08511.

(9) Arora, H.; Dong, R.; Venanzi, T.; Zscharchuch, J.; Schneider, H.; Helm, M.; Feng, X.; Cánovas, E.; Erbe, A. Demonstration of a Broadband Photodetector Based on a Two-Dimensional Metal-Organic Framework. *Adv. Mater.* **2020**, *32*, No. 1907063.

(10) Eagleton, A. M.; Ko, M.; Stolz, R. M.; Vereschchuk, N.; Meng, Z.; Mendecki, L.; Levenson, A. M.; Huang, C.; MacVeagh, K. C.; Mahdavi-Shakib, A.; Mahle, J. J.; Peterson, G. W.; Frederick, B. G.; Mirica, K. A. Fabrication of Multifunctional Electronic Textiles Using Oxidative Restructuring of Copper into a Cu-Based Metal-Organic Framework. *J. Am. Chem. Soc.* **2022**, *144*, 23297−23312.

(11) Yuan, K.; Song, T.; Yang, C.; Guo, J.; Sun, Q.; Zou, Y.; Jiao, F.; Li, L.; Zhang, X.; Dong, H.; Li, L.; Hu, W. Polymer-Assisted Space-Confined Strategy for the Foot-Scale Synthesis of Flexible Metal-Organic Framework-Based Composite Films. *J. Am. Chem. Soc.* **2021**, *143*, 17526−17534.

(12) Majidi, L.; Ahmadiparidari, A.; Shan, N.; Misal, S. N.; Kumar, K.; Huang, Z.; Rastegar, S.; Hemmat, Z.; Zou, X.; Zapol, P.; Cabana, J.; Curtiss, L. A.; Salehi-Khojin, A. 2D Copper Tetrahydroxyquinone Conductive Metal-Organic Framework for Selective CO_2 Electrocatalysis at Low Overpotentials. *Adv. Mater.* **2021**, *33*, No. 2004393.

(13) Nam, K. W.; Park, S. S.; Reis, R. D.; Dravid, V. P.; Kim, H.; Mirkin, C. A.; Stoddart, J. F. Conductive 2D Metal-Organic Framework for High-Performance Cathodes in Aqueous Rechargeable Zinc Batteries. *Nat. Commun.* **2019**, *10*, No. 4948.

(14) Huang, N. Y.; He, H.; Liu, S.; Zhu, H. L.; Li, Y. J.; Xu, J.; Huang, J. R.; Wang, X.; Liao, P. Q.; Chen, X. M. Electrostatic Attraction-Driven Assembly of a Metal-Organic Framework with a Photosensitizer Boosts Photocatalytic CO_2 Reduction to CO. *J. Am. Chem. Soc.* **2021**, *143*, 17424−17430.

(15) Meng, H.; Han, Y.; Zhou, C.; Jiang, Q.; Shi, X.; Zhan, C.; Zhang, R. Conductive Metal-Organic Frameworks: Design, Synthesis, and Applications. *Small Methods* **2020**, *4*, No. 2000396.

(16) Virmani, E.; Rotter, J. M.; Mähringer, A.; Zons, T. V.; Godt, A.; Bein, T.; Wuttke, S.; Medina, D. D. On-Surface Synthesis of Highly Oriented Thin Metal-Organic Framework Films through Vapor-Assisted Conversion. *J. Am. Chem. Soc.* **2018**, *140*, 4812−4819.

(17) Ma, Z. Z.; Li, Q. H.; Wang, Z.; Gu, Z. G.; Zhang, J. Electrically Regulating Nonlinear Optical Limiting of Metal-Organic Framework Film. *Nat. Commun.* **2022**, *13*, No. 6347.

(18) Giménez, V. R.; Galbiati, M.; Gil, J. C.; Barrios, N. A.; Sánchez, J. N.; Ariza, G. E.; Mattera, M.; Arnold, T.; Rawle, J.; Tatay, S.; Coronado, E.; Gastaldo, C. M. Bottom-Up Fabrication of Semiconductive Metal-Organic Framework Ultrathin Films. *Adv. Mater.* **2018**, *30*, No. 1704291.

(19) Yuan, K.; Song, T.; Zhu, X.; Li, B.; Han, B.; Zheng, L.; Li, J.; Zhang, X.; Hu, W. Construction of Large-Area Ultrathin Conductive Metal-Organic Framework Films through Vapor-Induced Conversion. *Small* **2019**, *15*, No. 1804845.

(20) Fu, Z.; Xu, G. Crystalline, Highly Oriented MOF Thin Film: the Fabrication and Application. *Chem. Rec.* **2017**, *17*, 518−534.

(21) Liu, Y.; Wei, Y.; Liu, M.; Bai, Y.; Wang, X.; Shang, S.; Du, C.; Gao, W.; Chen, J.; Liu, Y. Face-to-Face Growth of Wafer-Scale 2D Semiconducting MOF Films on Dielectric Substrates. *Adv. Mater.* **2021**, *33*, No. 2007741.

(22) Ikigaki, K.; Okada, K.; Tokudome, Y.; Toyao, T.; Falcaro, P.; Doonan, C. J.; Takahashi, M. MOF-on-MOF: Oriented Growth of Multiple Layered Thin Films of Metal-Organic Frameworks. *Angew. Chem.* **2019**, *131*, 6960−6964.

(23) Li, X.; Yu, J.; Jaroniec, M.; Chen, X. Cocatalysts for Selective Photoreduction of CO_2 into Solar Fuels. *Chem. Rev.* **2019**, *119*, 3962−4179.

(24) Litter, M. I. Heterogeneous Photocatalysis Transition Metal Ions in Photocatalytic Systems. *Appl. Catal. B: Environ.* **1999**, *23*, 89−114.

(25) Wu, T.; Liu, X.; Liu, Y.; Chen, M.; Liu, Z.; Zeng, G.; Shao, B.; Liang, Q.; Zhang, W.; He, Q.; Zhang, W. Application of QD-MOF

Composites for Photocatalysis: Energy Production and Environmental Remediation. *Coord. Chem. Rev.* **2020**, *403*, No. 213097.
(26) Kim, J. O.; Koo, W. T.; Kim, H.; Park, C.; Lee, T.; Hutomo, C. A.; Choi, S. Q.; Kim, D. S.; Kim, D.; Park, S. Large-Area Synthesis of Nanoscopic Catalyst-Decorated Conductive MOF Film Using Microfluidic-Based Solution Shearing. *Nat. Commun.* **2021**, *12*, No. 4294.
(27) Chen, L.; Luque, R.; Li, Y. Controllable Design of Tunable Nanostructures inside Metal-Organic Frameworks. *Chem. Soc. Rev.* **2017**, *46*, 4614−4630.
(28) Wang, M.; Xu, Y.; Peng, C. K.; Chen, S. Y.; Lin, Y. G.; Hu, Z.; Sun, L.; Ding, S.; Pao, C. W.; Shao, Q.; Huang, X. Site-Specified Two-Dimensional Heterojunction of Pt Nanoparticles/Metal-Organic Frameworks for Enhanced Hydrogen Evolution. *J. Am. Chem. Soc.* **2021**, *143*, 16512−16518.
(29) Zhao, M.; Deng, K.; He, L.; Liu, Y.; Li, G.; Zhao, H.; Tang, Z. Core-Shell Palladium Nanoparticle@Metal-Organic Frameworks as Multifunctional Catalysts for Cascade Reactions. *J. Am. Chem. Soc.* **2014**, *136*, 1738−1741.
(30) Zhao, M.; Yuan, K.; Wang, Y.; Li, G.; Guo, J.; Gu, L.; Hu, W.; Zhao, H.; Tang, Z. Metal-Organic Frameworks as Selectivity Regulators for Hyrogenation Reactions. *Nature* **2016**, *539*, 76−80.
(31) Ayala, A.; Carbonell, C.; Imaz, I.; Maspoch, D. Introducing Asymmetric Functionality into MOFs via the Generation of Metallic Janus MOF Particles. *Chem. Commun.* **2016**, *52*, 5096−5099.
(32) Zhao, M.; Chen, J.; Chen, B.; Zhang, X.; Shi, Z.; Liu, Z.; Ma, Q.; Peng, Y.; Tan, C.; Wu, X. J.; Zhang, H. Selective Epitaxial Growth of Oriented Hierarchical Metal-Organic Framework Heterostructures. *J. Am. Chem. Soc.* **2020**, *142*, 8953−8961.
(33) Gopinath, C. S.; Nalajala, N. A Scalable and Thin Film Approach for Solar Hydrogen Generation: a Review on Enhanced Photocatalytic Water Splitting. *J. Mater. Chem. A* **2021**, *9*, 1353−1371.
(34) Tudu, B.; Nalajala, N.; Reddy, K. P.; Saikia, P.; Gopinath, C. S. Electronic Integration and Thin Film Aspects of Au-Pd/rGO/TiO_2 for Improved Solar Hydrogen Generation. *ACS Appl. Mater. Interfaces* **2019**, *11*, 32869−32878.
(35) Wang, Q.; Hisatomi, T.; Jia, Q.; Tokudome, H.; Zhong, M.; Wang, C.; Pan, Z.; Takata, T.; Nakabayashi, M.; Shibata, N.; Li, Y.; Sharp, I. D.; Kudo, A.; Yamada, T.; Domen, K. Scalable Water Splitting on Particulate Photocatalyst Sheets with a Solar-to-Hydrogen Energy Conversion Efficiency Exceeding 1%. *Nat. Mater.* **2016**, *15*, 611−617.
(36) Nalajala, N.; Patra, K. K.; Bharad, P. A.; Gopinath, C. S. Why the Thin Film Form of a Photocatalyst is Better than the Particulate Form for Direct Solar-to-Hydrogen Conversion: a Poor Man's Approach. *RSC Adv.* **2019**, *9*, 6094−6100.
(37) Hmadeh, M.; Lu, Z.; Liu, Z.; Gándara, F.; Furukawa, H.; Wan, S.; Augustyn, V.; Chang, R.; Liao, L.; Zhou, F.; Perre, E.; Ozolins, V.; Suenaga, K.; Duan, X.; Dunn, B.; Yamamto, Y.; Terasaki, O.; Yaghi, O. M. New Porous Crystals of Extended Metal-Catecholates. *Chem. Mater.* **2012**, *24*, 3511−3513.
(38) Ouyang, T.; Wng, H. J.; Huang, H. H.; Wang, J. W.; Guo, S.; Liu, W. J.; Zhong, D. C.; Lu, T. B. Dinuclear Metal Synergistic Catalysis Boosts Photochemical CO_2-to-CO Conversion. *Angew. Chem., Int. Ed.* **2018**, *57*, 16480−16485.
(39) Manser, J. S.; Christians, J. A.; Kamat, P. V. Intriguing Optoelectronic Properties of Metal Halide Perovskites. *Chem. Rev.* **2016**, *116*, 12956−13008.
(40) Yao, M. S.; Lv, X. J.; Fu, Z. H.; Li, W. H.; Deng, W. H.; Wu, G. D.; Xu, G. Layer-by-Layer Assembled Conductive Metal-Organic Framework Nanofilms for Room-Temperature Chemiresistive Sensing. *Angew. Chem., Int. Ed.* **2017**, *56*, 16510−16514.
(41) Zhang, B.; Sun, L. Artificial Photosynthesis: Opportunities and Challenges of Molecular Catalysts. *Chem. Soc. Rev.* **2019**, *48*, 2216−2264.
(42) Zhong, D. C.; Gong, Y. N.; Zhang, C.; Lu, T. B. Dinuclear Metal Synergistic Catalysis for Energy Conversion. *Chem. Soc. Rev.* **2023**, *52*, 3170−3214.
(43) Ouyang, T.; Huang, H. H.; Wang, J. W.; Zhong, D. C.; Lu, T. B. A Dinuclear Cobalt Cryptate as a Homogeneous Photocatalyst for Highly Selective and Efficient Visible-Light Driven CO_2 Reduction to CO in CH_3CN/H_2O Solution. *Angew. Chem., Int. Ed.* **2017**, *56*, 738−743.
(44) Deacy, A. C.; Moreby, E.; Phanopoulos, A.; Williams, C. K. Co(III)/Alkali-Metal(I) Heterodinuclear Catalysts for the Ring-Opening Copolymerization of CO_2 and Propylene Oxide. *J. Am. Chem. Soc.* **2020**, *142*, 19150−19160.
(45) Qin, J.; Lei, N.; Zhu, H. L. Synthesis, Structural Characterization, Molecular Docking, and Urease Inhibition Studies of Dinuclear Cobalt(II) Complexes Derived from 3,5-Bis(pyridin-2-yl)-4-Amino-1,2,4-Triazole. *J. Coord. Chem.* **2014**, *67*, 1279−1289.
(46) Wu, L. Y.; Mu, Y. F.; Guo, X. X.; Zhang, W.; Zhang, Z. M.; Zhang, M.; Lu, T. B. Encapsulating Perovskite Quantum Dots in Iron-Based Metal-Organic Frameworks (MOFs) for Efficient Photocatalytic CO_2 Reduction. *Angew. Chem., Int. Ed.* **2019**, *58*, 9491−9495.
(47) Chen, Z.; Hu, Y.; Wang, J.; Shen, Q.; Zhang, Y.; Ding, C.; Bai, Y.; Jiang, G.; Li, Z.; Gaponik, N. Boosting Photocatalytic CO_2 Reduction on $CsPbBr_3$ Perovskite Nanocrystals by Immobilizing Metal Complexes. *Chem. Mater.* **2020**, *32*, 1517−1525.

https://doi.org/10.1021/jacs.3c14036
J. Am. Chem. Soc. 2024, 146, 6893−6904